BNL-228407-2025-JAAM

Enhancing Acidic Oxygen Evolution Activity by Controlling Oxidation State of Iridium

X. Han, P. Liu

To be published in "Angewandte Chemie"

June 2025

Chemistry Department

Brookhaven National Laboratory

U.S. Department of Energy

USDOE Office of Science (SC), Basic Energy Sciences (BES)

DISCLAIMER

Enhancing Acidic Oxygen Evolution Activity by Controlling Oxidation State of Iridium

Xue Han[a], ‡, Tianyou Mou[a], ‡, Sinwoo Kang[a], ‡, Arephin Islam[a], Xueru Zhao[a], Kotaro Sasaki[a], José A. Rodriguez[a], Qiaowan Chang[b], *, Ping Liu[a], *, Jingguang G. Chen[a], [c], *

[a] X. Han‡, T. Mou‡, S. Kang‡, A. Islam, X. Zhao, K. Sasaki, J. A. Rodriguez, P. Liu*, J. G. Chen*
Chemistry Division
Brookhaven National Laboratory
Upton, New York 11973, USA
E-mail: jgchen@columbia.edu
pingliu3@bnl.gov

[b] Q. Chang*
Gene and Linda Voiland School of Chemical Engineering and Bioengineering
Washington State University
Pullman, Washington 99164, USA
E-mail: qiaowan.chang@wsu.edu

[c] J. G. Chen*
Department of Chemical Engineering
Columbia University
New York, New York 10027, USA

[‡] These authors contributed equally to this work

Abstract: Iridium oxides with high oxidation states have been reported to be effective in enhancing the acidic oxygen evolution reaction (OER) performance. Herein, we develop ultrasmall IrO_x nanoparticles over titanium nitride, which undergoes surface oxidation under oxidative conditions to form oxygen-modified TiN (oxi-TiN), enabling the formation of highly oxidized $Ir^{\delta+}$ ($\delta > 4$). This IrO_x/oxi-TiN catalyst delivers higher Ir mass activity than commercial IrO_2, while comparable stability is maintained. The superior OER activity of IrO_x/oxi-TiN is further demonstrated in a proton exchange membrane water electrolyzer, requiring only 1.88 V to reach 3 A cm^{-2}, achieving the U.S. Department of Energy 2025 target (1.90 V at 3 A cm^{-2}). *In situ* X-ray absorption spectroscopy confirms that the superior OER activity of IrO_x/oxi-TiN originates from highly oxidized $Ir^{\delta+}$ under OER conditions. Density functional theory calculations reveal a general correlation between the oxidation state of Ir and OER overpotential. Specifically, the introduction of interfacial oxygen at the Ir/TiN interface increases the oxidation state of deposited $Ir^{\delta+}$ from $\delta < 4$ to $\delta > 4$, decreasing the OER overpotential. This study highlights the critical role of high oxidation states of $Ir^{\delta+}$ in enhancing OER activity, providing guidance for the development of advanced acidic OER catalysts.

Introduction

Designing active, stable, and lower-cost electrocatalysts for the acidic oxygen evolution reaction (OER) is critical for large-scale hydrogen production via proton exchange membrane (PEM) water electrolysis. [1-4] Currently, iridium oxide (IrO_x) is the only anode catalyst that meets the activity and stability requirements under the harsh OER environment in an acidic electrolyte. [5, 6] Recent literature reports suggest that the OER activity is related to the oxidation state of Ir, with high oxidation states of $Ir^{\delta+}$ ($\delta > 4$), such as Ir^{5+} or Ir^{6+}, being assumed to enhance the OER activity as demonstrated in examples like amorphous Li-IrO_x ($Ir^{>4+}$)[7], Sr_2CaIrO_6 ($Ir^{6+/5+}$)[8], Ir/NiFe ($Ir^{5.3+}$)[9], and atomically dispersed Ir^{6+} oxide[10]. However, the understanding of dependence between the oxidation state of Ir and the OER activity is rather limited, which hinders optimization of Ir-based catalysts for advanced acidic OER.

Recently, we employed the ethanol reduction method to deposit IrO_x nanoparticles (NPs) on titanium nitride (TiN), where the TiN surface is oxidized under oxidative conditions to form oxi-TiN (denoted as EtOH-IrO_x/oxi-TiN). This approach reduced the Ir loading to 30 wt% while maintaining acidic OER performance comparable to that of commercial IrO_2 (C-IrO_2). In this catalyst, the IrO_x NPs contain $Ir^{\delta+}$ ($1 < \delta < 4$).[11] In the current study, we report a carbon monoxide (CO)-assisted strategy to achieve highly oxidized $Ir^{\delta+}$ ($\delta > 4$) (denoted as CO-IrO_x/oxi-TiN). Compared to the ethanol-assisted method, the presence of CO is found to effectively reduce the size of Ir NPs from 1.58 nm to less than 1 nm and mitigate Ir aggregation. This is due to the fact that CO absorbs onto the Ir surface to limit and control particle growth due to its size-dependent chemisorption energy and coverage. [12, 13] The ultrasmall Ir clusters in CO-IrO_x/oxi-TiN result in an increased total interfacial contact area with the oxi-TiN support, enhancing the interfacial oxygen-to-Ir stoichiometry and thereby facilitating the formation of highly oxidized Ir species. *In situ* X-ray absorption spectroscopy (XAS) measurements further reveal that the oxidation state of Ir in CO-IrO_x/oxi-TiN exceeds Ir^{4+} under OER

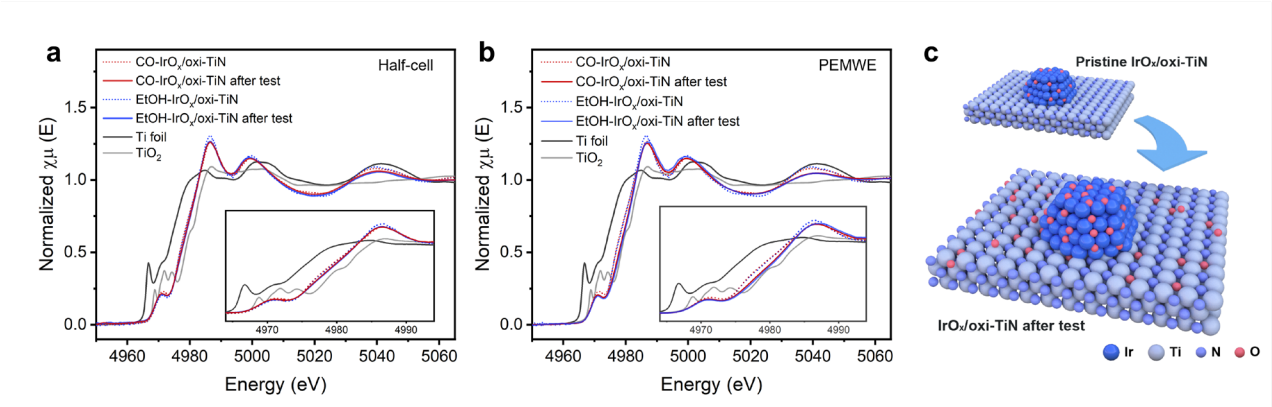

Figure 1. *Ex situ* Ti K-edge XANES spectra of CO-IrO_x/oxi-TiN and EtOH-IrO_x/oxi-TiN before and after (a) a stability test at 10 mA cm^{-2} in a half-cell; (b) a stability test at 200 mA cm^{-2} in a PEMWE. (c) Schematic illustration of pristine IrO_x/oxi-TiN structure and its structure after stability test.

potentials. The CO-IrO_x/oxi-TiN catalyst exhibits a low OER overpotential of 277 mV at the current density of 10 mA cm^{-2} and long-term stability in 100 hours continuous operation in an acid medium. With an Ir loading of 40 μg_{Ir} cm^{-2}, the mass activity of CO-IrO_x/oxi-TiN reaches 542 A g_{Ir}^{-1}, which is 6.3 times and 2.1 times higher than that of C-IrO_2 and EtOH-IrO_x/oxi-TiN, respectively. When integrated into a PEM water electrolyzer, the CO-IrO_x/oxi-TiN with a low iridium-loading of 0.26 mg cm^{-2} achieves a current density of 2.4 A cm^{-2} at 1.8 V using a Nafion membrane N212 at 60 °C, outperforming C-IrO_2 (1.2 A cm^{-2}) and EtOH-IrO_x/oxi-TiN (2.0 A cm^{-2}).

Density functional theory (DFT) calculations are further employed to understand the promoting effect of CO-IrO_x/oxi-TiN as compared to EtOH-IrO_x/oxi-TiN. A correlation between the oxidation state of Ir and the OER overpotential is established across a wide range of Ir-based catalysts including EtOH-IrO_x/oxi-TiN, IrO_x/Ir and IrO_2 in addition to CO-IrO_x/oxi-TiN. It is indicated that the oxidation state of Ir can serve as a descriptor for OER activity, with higher oxidation states generally being associated with lower OER overpotentials. The DFT results show that CO-IrO_x/oxi-TiN can enable the formation of higher stoichiometries of oxygen/Ir than that of EtOH-IrO_x/oxi-TiN and C-IrO_2, thus facilitating oxidation of Ir and enabling selective bond-tuning to reduce the OER overpotential. Overall, this work highlights the effective tuning of oxidation state of Ir by a size controllable CO-mediated synthetic method to enhance catalytic activity, while maintaining stability under acidic OER conditions.

Results and Discussion

To determine whether the TiN support was partially oxidized during OER, *ex situ* Ti K-edge X-ray absorption near-edge structure (XANES) measurements were conducted on EtOH-IrO_x/oxi-TiN and CO-IrO_x/oxi-TiN catalysts before and after a 100-hour stability test at 10 mA cm^{-2} in a half-cell and a 2-hour stability test at 200 mA cm^{-2} in a proton exchange membrane water electrolyzer (PEMWE). The Ti K-edge XANES spectra of both catalysts (**Figure 1a**) show a slight shift of the absorption edge toward higher energy after a 10 mA cm^{-2} half-cell test. A more significant energy shift is observed during the stability test at a higher current density of 200 mA cm^{-2} in the PEMWE (**Figure 1b**). These observations suggest that the TiN surface is partially oxidized to oxi-TiN under oxidative conditions. A schematic illustration of the pristine IrO_x/oxi-TiN structure and its structure after the OER stability test is shown in **Figure 1c**. It is recognized that the particle size of metal catalysts affects its interaction with the support surface.[14] Specifically, smaller Ir clusters should enhance the interaction with surface oxygen on oxi-TiN. The CO-assisted synthetic method is herein employed to reduce the size of Ir. The resulting smaller Ir clusters enhance the interfacial interaction between oxi-TiN and the supported Ir, aiming to increase the O/Ir stoichiometry at the interface under OER conditions, thereby achieving a high oxidation state of $Ir^{\delta+}$ ($\delta > 4$) to enhance the OER activity.

The transmission electron microscopy (TEM) images (**Figure 2a and S1)** show that the IrO_x NPs in EtOH-IrO_x/oxi-TiN, from the conventional synthesis method of ethanol reduction[11], are partially aggregated with an average size of 1.58 nm (**Figure 2b**). In contrast, when the catalyst is synthesized under a CO atmosphere, the IrO_x NPs in CO-IrO_x/oxi-TiN are uniformly dispersed on the support, with the average size of IrO_x being reduced to 0.91 nm, indicating that the presence of CO effectively confines the Ir particle size. High-angle annular dark-field scanning TEM (HAADF-STEM) and the corresponding X-ray energy dispersive spectroscopy (EDS) mapping were performed to gain insight into the distribution of Ir, Ti, N, and O in the catalysts. EDS mapping of Ir in EtOH-IrO_x/oxi-TiN (**Figure S2**) shows particle aggregation, and the EDS quantitative measurement yields a mass loading of ~30 wt% Ir (**Table S1**). In contrast, EDS mapping of CO-IrO_x/oxi-TiN (**Figure 2c**) reveals a uniform dispersion of Ir, with the Ir loading estimated to be ~20 wt% (**Table S1**).

The powder X-ray diffraction (XRD) pattern of EtOH-IrO_x/oxi-TiN shows a peak at 2θ=41°, corresponding to metallic Ir with

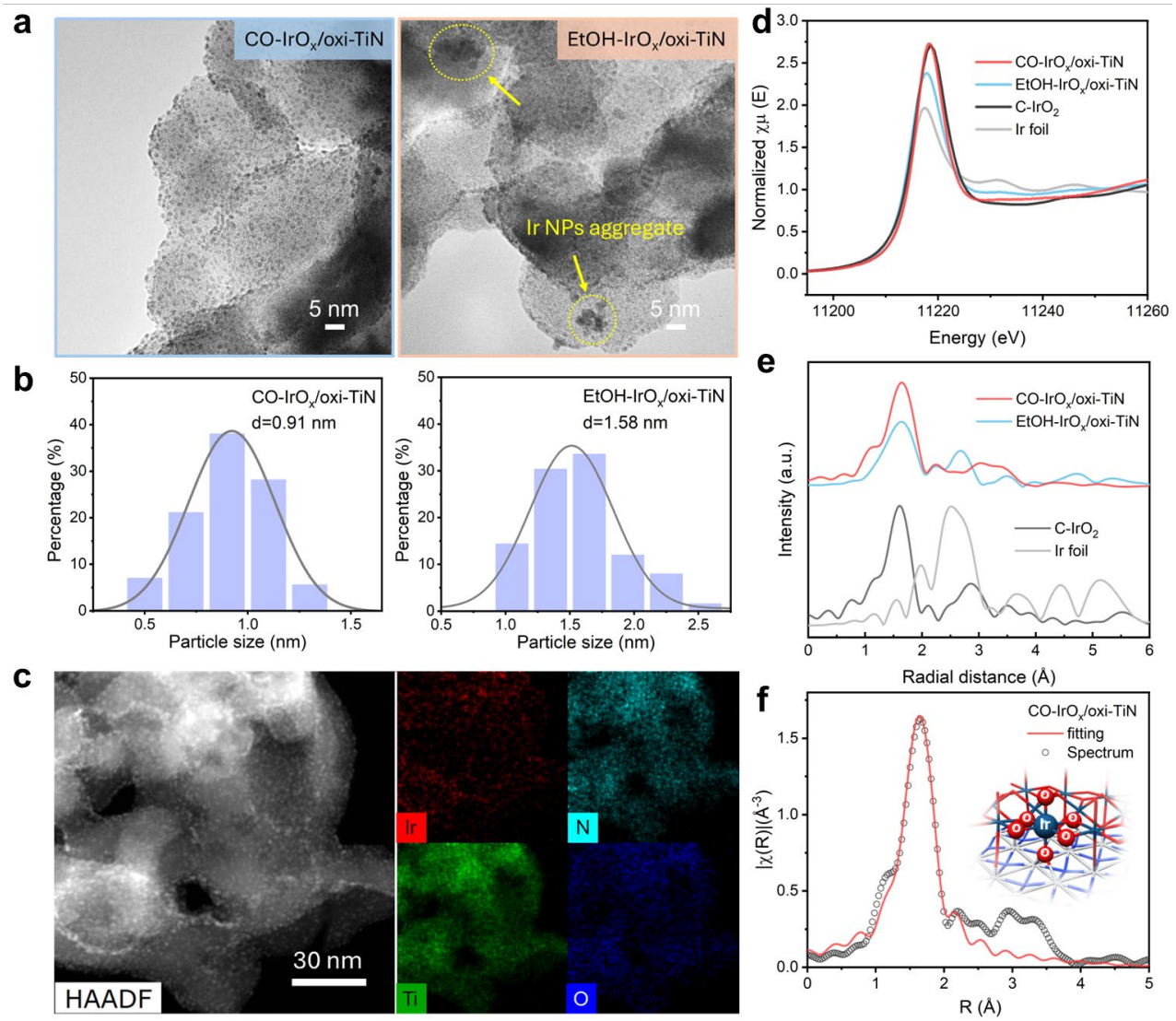

Figure 2. Morphology and structural characterization. (a) TEM images of CO-IrO_x/oxi-TiN and EtOH-IrO_x/oxi-TiN and (b) the corresponding particle size distribution of Ir. (c) HAADF-STEM image of CO-IrO_x/oxi-TiN and the corresponding EDS mappings. (d) Ir L_3-edge XANES spectra of CO-IrO_x/oxi-TiN and other reference materials. (e) Fourier transformation of the EXAFS spectra of CO-IrO_x/oxi-TiN and other reference materials. (f) first-shell fitting curves for CO-IrO_x/oxi-TiN.

face-centered cubic crystal structure. In comparison, the XRD pattern of CO-IrO_x/oxi-TiN shows a broad peak at 2θ=33° that matches well with the diffraction peak of amorphous C-IrO_2 (**Figure S3**). This peak shows weak intensity, consistent with the sub-nanometer size of the IrO_x particles. The X-ray photoelectron spectroscopy (XPS) measurements were carried out to understand the oxidation state of catalysts (**Figure S4 and S5)**. The Ir 4f XPS spectrum of EtOH-IrO_x/oxi-TiN can be deconvoluted into two sets of peaks at 60.3 and 61.1 eV for 4f 7/2, and at 63.3 and 64.1 eV for 4f 5/2, attributed to metallic Ir^0 and Ir^{4+}, respectively, demonstrating a mixed oxidation state of Ir. In contrast, the Ir 4f spectrum of CO-IrO_x/oxi-TiN can only be deconvoluted into two peaks at 61.9 and 64.9 eV, which are attributed to Ir^{4+}, indicating that Ir is fully oxidized due to the smaller particle size. *Ex situ* XAS was employed to further investigate the oxidation state and local atomic environment of IrO_x/oxi-TiN catalysts. The energy position of the white line in XANES at the 5d transition metals is typically related to their oxidation states. [1] As shown in **Figure 2d**, the position of the white line in the Ir L_3-edge XANES spectrum for EtOH-IrO_x/oxi-TiN is situated between those of Ir foil and C-IrO_2 references, suggesting that the oxidation state of Ir in EtOH-IrO_x/oxi-TiN ranges from Ir^0 and Ir^{4+}. The white line position of CO-IrO_x/oxi-TiN shifts by 0.9 eV to a higher energy compared to the Ir foil reference but is located at the similar energy position to C-IrO_2, indicating the average oxidation state of Ir is close to Ir^{4+}. The XANES results of EtOH-IrO_x/oxi-TiN and CO-IrO_x/oxi-TiN are consistent with their XPS results. Furthermore, the Ir L_3-edge extended X-ray

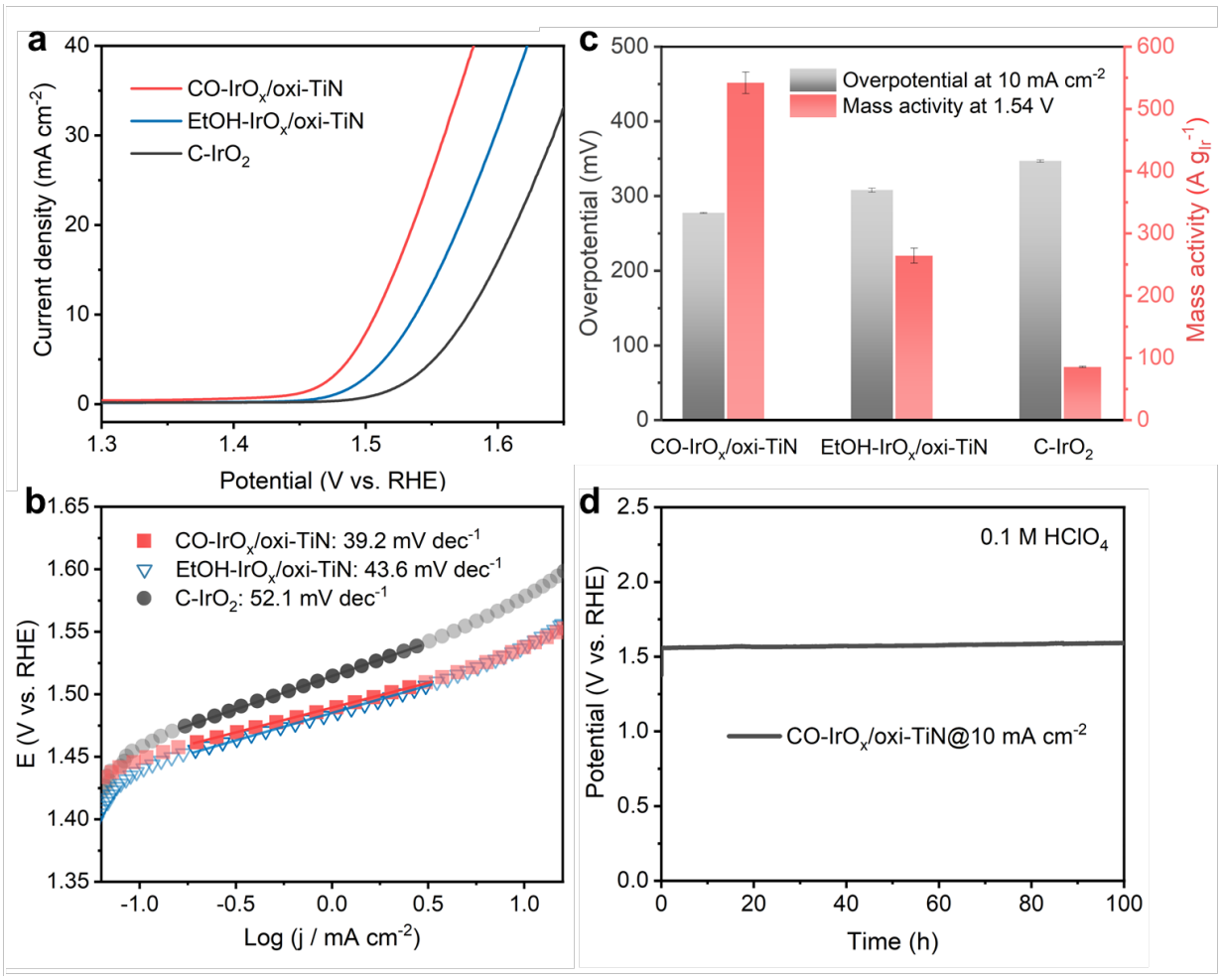

Figure 3. Electrochemical OER performance of CO-IrO_x/oxi-TiN, EtOH-IrO_x/oxi-TiN, and C-IrO_2 at half-cell RDE set-up. (a) OER polarization curves; (b) Tafel plots. (c) Comparison of overpotential and mass activity of CO-IrO_x/oxi-TiN, EtOH-IrO_x/oxi-TiN, and C-IrO_2 at 10 mA cm^{-2} and at 1.54 V. (d) Stability test of CO-IrO_x/oxi-TiN catalyst at a current density of 10 mA cm^{-2}.

absorption fine structure (EXAFS) of EtOH-IrO_x/oxi-TiN (**Figure 2e**) shows two peaks, with the first peak attributed to the Ir-O bond and a minor second peak corresponding to the metallic Ir-Ir bond. For comparison, the EXAFS result of CO-IrO_x/oxi-TiN at the Ir L_3-edge exhibits a dominant peak at 1.63 Å corresponding to the Ir-O bond. Additionally, no metallic Ir peak is observed in the spectrum, indicating that Ir species are fully oxidized. The EXAFS fitting result of CO-IrO_x/oxi-TiN (**Figure 2f and Table S4**) further confirms that the coordination number (CN) of Ir-O is 5.6, similar to the C-IrO_2 standard, which has a CN of 6. This suggests that the oxidation state of Ir in CO-IrO_x/oxi-TiN is 4+, with Ir coordinates with six O atoms. Overall, the *ex situ* XPS, XANES, and EXAFS results demonstrate that Ir clusters with larger sizes in EtOH-IrO_x/oxi-TiN exhibit a mixed oxidation state of Ir^0 and Ir^{4+}, whereas smaller Ir clusters in CO-IrO_x/oxi-TiN are oxidized to Ir^{4+}.

The OER performances of CO-IrO_x/oxi-TiN were evaluated in 0.1 M $HClO_4$ electrolyte using a rotating disk electrode (RDE) set-up. For comparison, the catalytic activity of EtOH-IrO_x/oxi-TiN and the benchmark C-IrO_2 is also measured with the same Ir loading on the electrode. All measured potentials in this work were calibrated to the reversible hydrogen electrode (RHE) and the current densities were normalized to the geometric area of the RDE. Linear sweep voltammetry (LSV) curves (**Figure 3a**) show that CO-IrO_x/oxi-TiN with an Ir loading of 40 μg_{Ir} cm^{-2} exhibits an overpotential of 277 mV at a current density of 10 mA cm^{-2}, which is lower than EtOH-IrO_x/oxi-TiN (308 mV) and C-IrO_2 (347 mV) with the same Ir loading. The effect of Ir loading is also compared by increasing the loading to 100 μg_{Ir} cm^{-2}. As shown in **Figure S6**, the overpotentials of CO-IrO_x/oxi-TiN with 40 and 100 µg of Ir correspond to 277 and 256 mV at 10 mA cm^{-2}, respectively, demonstrating competitive performance compared to recent reports on Ir-based catalysts for acidic OER (**Table S2**). The enhanced OER activity of CO-IrO_x/oxi-TiN is also revealed by the Tafel slope of 39.2 mV dec^{-1}, suggesting that this catalyst has faster kinetics than EtOH-IrO_x/oxi-TiN (43.6 mV dec^{-1}) and C-IrO_2 (52.1 mV dec^{-1}) (**Figure 3b**). The electrochemical active surface area (ECSA) was calculated from double-layer capacitance (C_{dl}) measurements, as shown in **Figure S7**. By normalizing the OER current density to ECSA at 1.54 V (**Figure S8**), CO-IrO_x/oxi-TiN exhibits the highest specific activity (0.111 mA cm^{-2}_{ECSA}), compared to EtOH-IrO_x/oxi-TiN (0.071 mA cm^{-2}_{ECSA}) and C-IrO_2

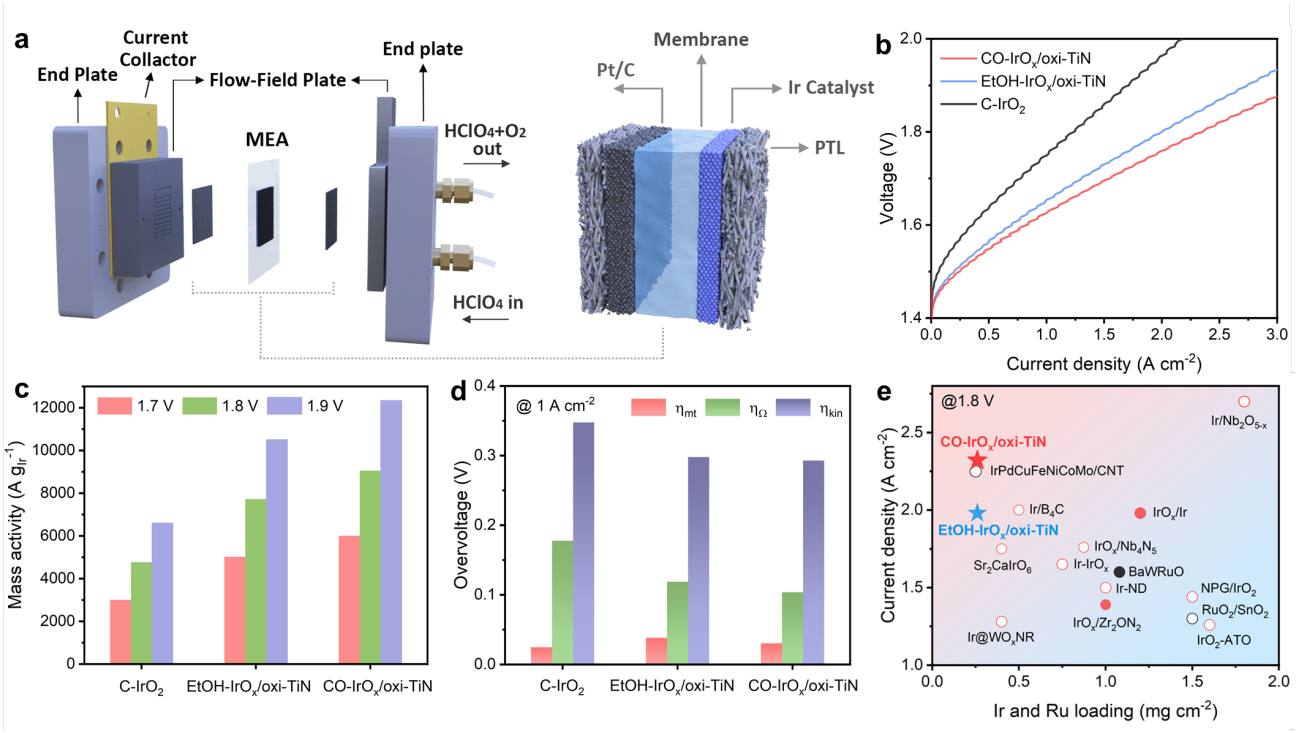

Figure 4. Electrochemical measurements of CO-IrO_x/oxi-TiN, EtOH-IrO_x/oxi-TiN, and C-IrO_2 in PEMWE cell. (a) Schematic illustration of PEMWE and MEA structures. (b) I-V curve. (c) Mass activity comparison at 1.7, 1.8, and 1.9 V. (d) Overvoltage deconvolution of the I-V curve of different catalysts. (e) Activity comparison at 1.8 V with state-of-the-art reports. ($★_{red/blue}$: This study, $●_{red}$: Acid electrolyte with Ir-based catalyst, $○_{red}$: DI water with Ir-based catalyst, $●_{Black}$: Acid electrolyte with Ru-based catalyst, $○_{Black}$: DI water with Ru-based catalyst)

($0.013\ mA\ cm^{-2}_{ECSA}$). The mass activity was calculated under the same Ir mass loading at the electrode. In **Figure 3c** and **Figure S9**, CO-IrO_x/oxi-TiN exhibits the highest mass activity of 542 A g_{Ir}^{-1} at 1.54 V, which is 2.1 and 6.3 times higher than EtOH-IrO_x/oxi-TiN (264.3 A g_{Ir}^{-1}) and C-IrO_2 (85.5 A g_{Ir}^{-1}), respectively. In addition to activity, long-term stability is another critical criterion to evaluate the electrocatalyst performance under acidic OER conditions. The stability of the CO-IrO_x/oxi-TiN catalyst was evaluated using chronopotentiometry (CP) measurements at 10 mA cm^{-2}. As shown in **Figure 3d**, CO-IrO_x/oxi-TiN shows long-term stability for 100 hours of continuous operation, with negligible potential degradation. While C-IrO_2, used as a reference, shows rapid degradation after 80 hours (**Figure S10**), likely due to the instability of the carbon paper substrate. In addition, the TEM images of CO-IrO_x/oxi-TiN after the OER test (**Figure S11**) show that the catalyst still maintains the original morphology and structure. *Ex situ* XAENS analyses were employed to identify the oxidation state of Ir after the OER test. As shown in **Figure S12**, the white line peak position shifts toward higher energy compared to the pristine catalyst, indicating the formation of highly oxidized Ir species ($Ir^{\delta+}$, $\delta > 4$). Notably, such a high oxidation state is maintained above Ir^{4+} even after the OER process.

Proton exchange membrane water electrolysis measurements were conducted using a membrane electrode assembly (MEA) (**Figure 4a**). Commercial Pt/C (1.0 $mg_{Pt}\ cm^{-2}$) was coated on the membrane for the cathode, while IrO_x catalysts ($0.26\ mg_{Ir}\ cm^{-2}$) were loaded onto the substrate (**details provided in the Supplemental Information**). The rates of electrochemical oxygen and hydrogen production, along with the current-voltage (I-V) curve (without iR compensation), were measured in a two-electrode zero-gap configuration at 60 °C using 0.1 M $HClO_4$. CO-IrO_x/oxi-TiN exhibited the highest activity (2.4 A cm^{-2}) at 1.8 V, outperforming EtOH-IrO_x/oxi-TiN (2.0 A cm^{-2}) and C-IrO_2 (1.2 A cm^{-2}) (**Figure 4b**). This is consistent with a two-fold increase in the hydrogen production rate for CO-IrO_x/oxi-TiN, reaching 6.11 L h^{-1}, compared to C-IrO_2 (3.05 L h^{-1}), as calculated from the OER current. The mass activity of CO-IrO_x/oxi-TiN reached 9050 A g_{Ir}^{-1} at 1.8 V, a higher value than EtOH-IrO_x/oxi-TiN (7721 A g_{Ir}^{-1}) and C-IrO_2 (4763 A g_{Ir}^{-1}) (**Figure 4c**). This result highlights the necessity of applying MEA, as it enhances Ir utilization by an order of magnitude compared to the mass activity of CO-IrO_x/oxi-TiN (542 A g_{Ir}^{-1}) observed in half-cell measurements. Overvoltage analysis was performed to distinguish contributions of kinetic (η_{kin}), Ohmic (η_Ω), and mass transport (η_{mt}) losses to the I-V curves (**Figure 4d**). The total overvoltage decreased in CO-IrO_x/oxi-TiN (0.427 V) compared to C-IrO_2 (0.550 V) at 1 A cm^{-2}. The primary factors contributing to this reduction were η_{kin} (CO-IrO_x/oxi-TiN: 0.293 V; C-IrO_2: 0.348 V) and η_Ω (CO-IrO_x/oxi-TiN: 0.103 V; C-IrO_2: 0.178 V), while η_{mt} showed negligible changes. This finding aligns with high-frequency resistance (HFR) measurements using electrochemical impedance spectroscopy, where CO-IrO_x/oxi-TiN (23.5 mΩ) exhibited a lower Ohmic resistance than C-IrO_2 (33.1 mΩ) at 0.1 A cm^{-2} (**Figure S13**). The stability test at 200 mA cm^{-2}

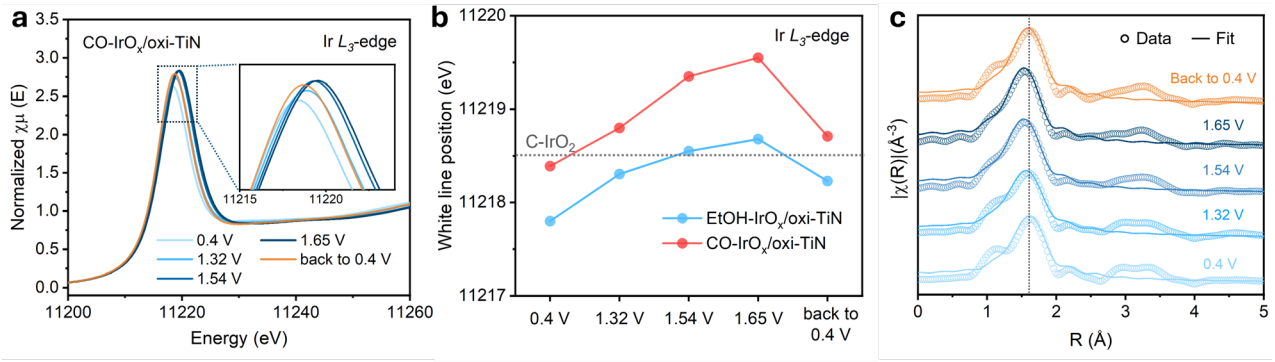

Figure 5. *In situ* XAS characterization. (a) *In situ* Ir L_3-edge XANES spectra of CO-IrO_x/oxi-TiN under various applied potentials. (b) The white line position of CO-IrO_x/oxi-TiN and EtOH-IrO_x/oxi-TiN at various potentials. (c) First-shell fitting of Ir L_3-edge EXAFS spectra for CO-IrO_x/oxi-TiN.

using CP measurement demonstrated a comparable stability of the CO-IrO_x/oxi-TiN and EtOH-IrO_x/oxi-TiN catalysts with C-IrO_2 over 100 hours (**Figure S14**). The outstanding performance of CO-IrO_x/oxi-TiN (1.88 V at 3 A cm^{-2}) surpasses recent state-of-the-art PEMWE benchmarks and exceeds the United States Department of Energy's 2025 target [15] (1.90 V at 3 A cm^{-2}) (**Figure 4b and 4e**). [8, 16-26]

Additionally, to investigate the effect on the formation of oxi-TiN in PEMWE, CP measurements (**Figure S15**) were performed at 200 mA cm^{-2} for 2-hour in 0.1 M $HClO_4$. As shown in **Figure S16**, the HFR of both CO-IrO_x/oxi-TiN and EtOH-IrO_x/oxi-TiN increases by 2 mΩ after a 2-hour stability test, suggesting the formation of a less conductive oxide phase. This observation is consistent with the Ti K-edge XANES spectra (**Figure 1b**), which indicate that TiN is partially oxidized to oxi-TiN during continuous operation. Notably, even though TiN converts to oxi-TiN under oxidative conditions, the CO-IrO_x/oxi-TiN and EtOH-IrO_x/oxi-TiN catalysts still exhibit negligible degradation during the operation. This suggests that the formation of oxi-TiN during OER has a minimal effect on the overall catalytic performance.

To further understand the excellent OER catalytic performance of CO-IrO_x/oxi-TiN, the dynamic changes in the Ir oxidation state and local coordination environment were probed using *in situ* XAS at potentials of 0.4 V, 1.32 V, 1.54 V, 1.65 V and then back to 0.4 V. As shown in **Figure 5a**, the Ir L_3-edge XANES spectra of CO-IrO_x/oxi-TiN show a gradually increased white line energy position when the applied potential is stepped from 0.4 V to 1.65 V, with an energy shift of 1.16 eV, suggesting that Ir is oxidized to a higher oxidation state. When the applied potential is reversed to 0.4 V, the peak position shifts to a lower energy but it is still higher than the initial value at 0.4 V, indicating that the oxidation state change in CO-IrO_x/oxi-TiN is irreversible. Similarly, EtOH-IrO_x/oxi-TiN (**Figure S17**) exhibits the same trend in white line energy shift as CO-IrO_x/oxi-TiN with increasing applied potential. However, its energy shift from 0.4 V to 1.65 V is only 0.86 eV, suggesting a smaller increase in the Ir oxidation state compared to CO-IrO_x/oxi-TiN. The white line energy positions for CO-IrO_x/oxi-TiN and EtOH-IrO_x/oxi-TiN at each potential are compared in **Figure 5b**, showing that the energy position of EtOH-IrO_x/oxi-TiN remains lower than CO-IrO_x/oxi-TiN at all applied potentials. Notably, the white line energy of CO-IrO_x/oxi-TiN increases rapidly at high OER potentials (i.e., 1.54 V and 1.65 V), significantly higher than that of EtOH-IrO_x/oxi-TiN and the C-IrO_2 standard (gray dotted line), confirming a transition of Ir from Ir^{4+} to a more catalytically active $Ir^{\delta+}$ (δ>4).

The *in situ* Ir L_3-edge EXAFS fitting results of EtOH-IrO_x/oxi-TiN (**Figure S18, S19** and **Table S3**) show two peaks associated with the Ir-O bond and Ir-Ir bond at 0.4 V. The Ir-Ti bonds are observed between IrO_x and TiN when the potential increases to 1.32 V and above (**Table S3**). By comparison, the EXAFS fitting results of CO-IrO_x/oxi-TiN (**Figure 5c, Figure S20, S21** and **Table S4**) show a peak corresponding to the Ir-O bond, with a bond length of 2.02 Å and a CN of 5.5±0.8 at the applied potential of 0.4 V. As the potential increases from 0.4 V to 1.65 V, the CN remains unchanged, while the bond length of Ir-O decreases by 0.08 Å. Combined with the increase in white line energy in XANES, this indicates the formation of stronger Ir-O bonds between Ir and the oxi-TiN surface, consistent with an increase in the Ir oxidation state. Notably, Ir-Ti bonds are not detected in CO-IrO_x/oxi-TiN under OER potentials. This implies the formation of an oxygen layer between Ir and TiN, which prevents the Ir-Ti bond formation. Overall, the *in situ* XAS results reveal that EtOH-IrO_x/oxi-TiN with larger Ir cluster size exhibits a lower oxidation state of Ir, along with the presence of Ir-O, Ir-Ir, and Ir-Ti bonds. While CO-IrO_x/oxi-TiN with smaller Ir clusters increases the Ir-O bond strength between interfacial oxygen and Ir at the interface, thereby facilitating the formation of a high oxidation state of $Ir^{\delta+}$ (δ>4) under OER conditions, corresponding to an enhanced OER activity.

DFT calculations were performed to gain insight into the enhanced OER activity of CO-IrO_x/oxi-TiN over EtOH-IrO_x/oxi-TiN and C-IrO_2 observed experimentally. To describe CO-IrO_x/oxi-TiN, one to three monolayers (ML) of rutile IrO_2(110)-like conformation were placed on oxygen-covered TiN(100) (denoted as 1ML-$IrO_{x(x>2)}$/oxi-TiN, 2ML-$IrO_{x(x>2)}$/oxi-TiN, and 3ML-$IrO_{x(x>2)}$/oxi-TiN, **Figures 6a-c, S22** and **S23**). These models not only describe the

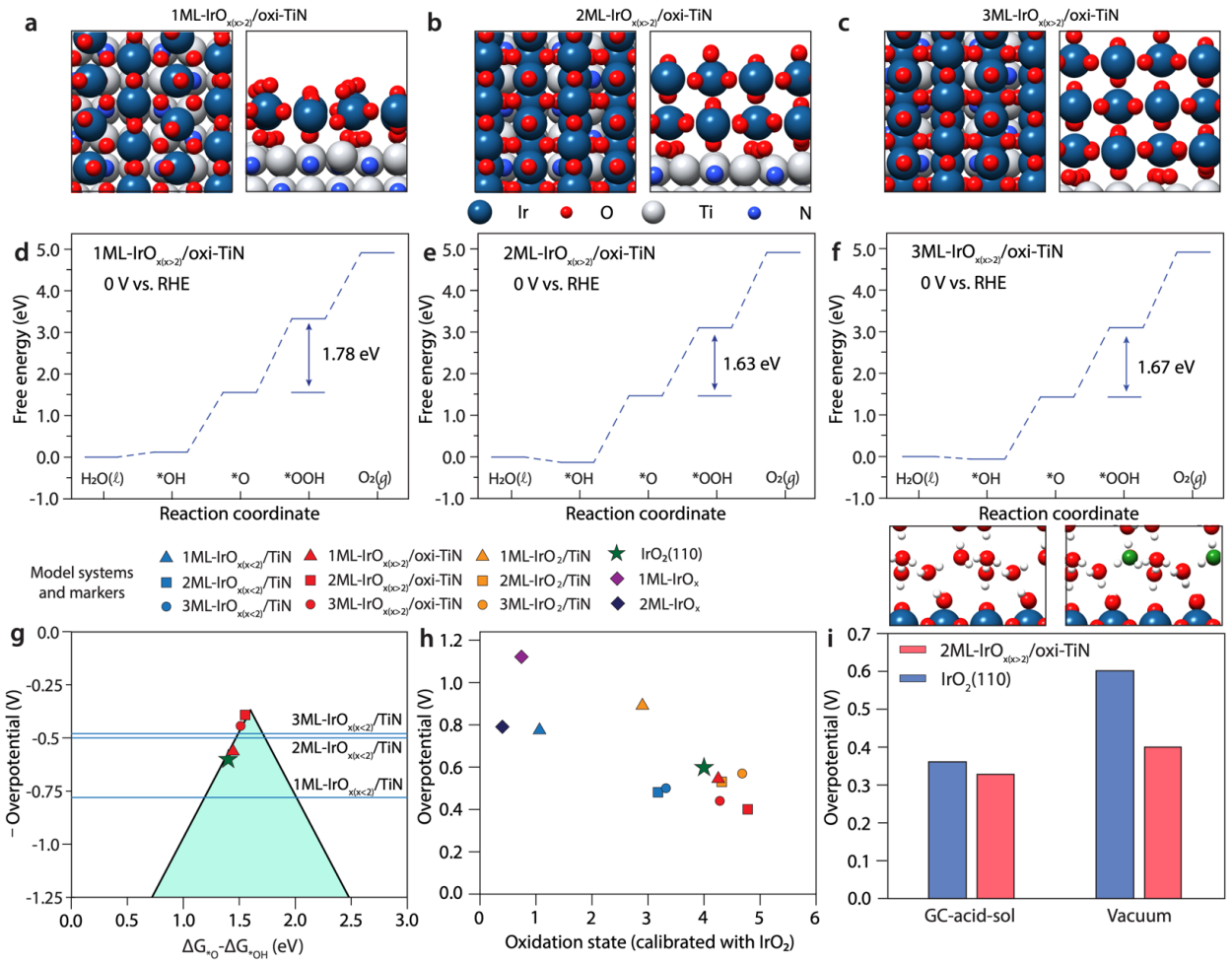

Figure 6. Top (left) and side (right) view of (a) 1ML-IrO$_{x(x>2)}$/oxi-TiN, (b) 2ML-IrO$_{x(x>2)}$/oxi-TiN, and (c) 3ML-IrO$_{x(x>2)}$/oxi-TiN interface models optimized using DFT. For detailed structures see **Figure S22**. DFT-calculated free energy diagrams for acidic OER on (d) 1ML-IrO$_{x(x>2)}$/oxi-TiN, (e) 2ML-IrO$_{x(x>2)}$/oxi-TiN, and (f) 3ML-IrO$_{x(x>2)}$/oxi-TiN. (g) Volcano plot of the negative value of overpotential (-η) versus the Gibbs free adsorption energy difference of *O and *OH ($\Delta G_{*O} - \Delta G_{*OH}$). Three IrO$_{x(x>2)}$/oxi-TiN systems were included, and with IrO$_2$ plotted as a green star. For comparison, 2ML-IrO$_{x(x<2)}$/TiN systems, which prefer the SOM and are not suitable for using $\Delta G_{*O} - \Delta G_{*OH}$ as the descriptor, were shown as blue lines for reference. (h) Overpotential (η) versus the oxidation state calibrated with IrO$_2$. Twelve model systems were included. (i) Comparison between the overpotential for 2ML-IrO$_{x(x>2)}$/oxi-TiN and IrO$_2$(110) systems using grand-canonical DFT with acidified solvation (GC-acid-sol) and vacuum methods.[31] See **SI** for details of different methods.

highly oxidized IrO$_{x(x>2)}$ under acidic OER reaction conditions (> 1.5 V vs. RHE),[24, 27, 28] but also capture the absence of Ir-Ir and Ir-Ti bonds as observed by *in situ* XAS (**Figure 5**). Wherein, the strain in the supported IrO$_x$ layer was limited to 0.3%. Notably, IrO$_x$ overlayers were employed to represent the terrace active sites of the IrO$_x$ nanoparticles observed experimentally (**Figure 2a**), since the edge and corner sites were found to be less active for the OER (**Table S5**).[11] The EtOH-IrO$_x$/oxi-TiN catalysts were considered for comparison, featuring the partially oxidized IrO$_{x(x<2)}$ over TiN(100) with the Ir-Ir and Ir-Ti bonds at the interface as reported previously (denoted as IrO$_{x(x<2)}$/TiN, **Figure S24**).[11] The IrO$_2$(110) surface (IrO$_2$, **Figure S25**) was also included to model C-IrO$_2$ as a benchmark.

According to the DFT-calculated potential free energy diagram at zero potential (0 V, **Figures 6d-f, S26** and **S27**), three IrO$_{x(x>2)}$/oxi-TiN systems prefer the adsorbate evolution mechanism (AEM) mechanism as reported for IrO$_2$(110) (**Figure S27**).[11, 24, 29] The coordinatively unsaturated Ir site (Ir$_{CUS}$) and bridging O (O$_{BR}$) site participate in the reaction directly. Specifically, the reaction is initiated by a vacant CUS to allow the adsorption and dissociation of H$_2$O into *OH$_{CUS}$, which is followed by the deprotonation of *OH$_{CUS}$ to *O$_{CUS}$. The *O$_{CUS}$ then forms *OOH$_{CUS}$ via the nucleophilic attack of H$_2$O. The deprotonation of *OOH$_{CUS}$ produces *OO$_{CUS}$, which spontaneously desorbs to form an O$_2$ molecule. The potential determining step (PDS) that corresponds to the maximum free energy change (ΔG_{max}) among the elementary steps is identified as the nucleophilic attack of H$_2$O to form *OOH$_{CUS}$.[27] The surface oxygen-participating mechanism (SOM) is favored for IrO$_{x(x<2)}$/TiN systems due to the weak binding of *OOH (**Table S5**)[11], where the PDS changes from the HO-O

coupling to H_2O dissociation with the increasing of IrO_x layer from 1ML to 3ML (**Figure S28** and **S29**).

The OER overpotential (η) was estimated based on the DFT-predicted ΔG_{max}. The 2ML-$IrO_{x(x>2)}$/oxi-TiN (η = 0.40 eV) system displays the lowest overpotential, followed by 3ML-$IrO_{x(x>2)}$/oxi-TiN (η = 0.44 eV) < 3ML-$IrO_{x(x<2)}$/TiN (η = 0.48 eV) < 2ML-$IrO_{x(x<2)}$/TiN (η = 0.50 eV) < 1ML-$IrO_{x(x>2)}$/oxi-TiN (η = 0.55 eV) < IrO_2 (η = 0.60 eV) < 1ML-$IrO_{x(x<2)}$/TiN (η = 0.78 eV) (**Figures 6d-f** and **S28**). Considering the results for 2ML- and 3ML-$IrO_{x(x<2)}$/TiN, DFT calculations confirm the decreasing trend in OER activity going from $IrO_{x(x>2)}$/oxi-TiN, $IrO_{x(x<2)}$/TiN, to IrO_2, consistent with the trend observed experimentally (**Figure 3a**). The 1ML-$IrO_{x(x<2)}$/TiN and 1ML-$IrO_{x(x>2)}$/oxi-TiN systems show lower stability than the counterparts with 2ML and 3ML due to higher formation energy (**Table S6**) and thus are less representative for the synthesized catalysts.

The decrease in OER overpotential from IrO_2 to $IrO_{x(x>2)}$/oxi-TiN is captured by the binding energy difference between *O and *OH (ΔG_{*O}-ΔG_{*OH}) via a volcano-like relationship, which has been used to describe the AEM-dominated OER activity over metal oxide catalysts (**Figure 6g**). [30] The formation of $IrO_{x(x>2)}$/oxi-TiN provides more oxidized Ir_{CUS} sites, enabling selective stabilization of *OH and thus *OOH species over *O to facilitate the PDS (**Figure 6g, h** and **Table S8**). This promoting effect increases from 1ML-$IrO_{x(x>2)}$/oxi-TiN to 2ML-$IrO_{x(x>2)}$/oxi-TiN and 3ML-$IrO_{x(x>2)}$/oxi-TiN. With the higher oxidation state of the Ir_{CUS} site, $IrO_{x(x>2)}$/oxi-TiN systems are also more active than the counterpart $IrO_{x(x<2)}$/TiN (**Figure 6h**). This is attributed to the selective tuning of the binding energy, where *OH binding on $IrO_{x(x>2)}$/oxi-TiN is selectively stabilized compared to $IrO_{x(x<2)}$/TiN, leading to a shift in the reaction mechanism from SOM to AEM.

A clear dependence of OER overpotential on the oxidation state of surface $Ir^{\delta+}$ is established based on the results for $IrO_{x(x>2)}$/oxi-TiN in this study as well as other referenced models, including $IrO_{x(x<2)}$/TiN, IrO_x/Ir and IrO_2 (See **SI** for detailed structures and energetics, **Figure S30** and **S31**). In general, to achieve a higher OER activity than IrO_2, a higher oxidation state of $Ir^{\delta+}$ ($\delta > 4$) is essential, as seen for the $IrO_{x(x>2)}$/oxi-TiN, and the 3ML-, 2ML-IrO_2/TiN (**Figure 6h** and **Table S8**). Saturation of oxygen over TiN(100) offers a high stoichiometry of surface O relative to Ir, leading to the highest oxidation state and therefore the lowest OER overpotential. Exceptions are seen for 2ML-, 3ML-$IrO_{x(x<2)}$/TiN. Although the oxidation state of $Ir^{\delta+}$ is slightly lower than 4+, the activity is still higher than IrO_2. This is likely associated with structural flexibility of these nanostructures, which distort upon interaction with strong reaction intermediates, e.g. *O and *OH. As a result, the oxidation states estimated based on the bare surfaces may not fully reflect those under reaction conditions.

According to the oxidation state-overpotential relationship (**Figure 6h**), oxidation of oxygen-covered TiN(100) to TiO_yN_{1-y}(100) by replacing the first layer of N into O (denoted as oxi-TiO_yN_{1-y}, **Figure S32**) was considered, seeking the possibility to further increase the oxidation state of $Ir^{\delta+}$ on the surface. However, according to DFT calculations, the oxidation state is barely affected. In addition, the structure and reaction mechanism of $IrO_{x(x>2)}$/oxi-TiO_yN_{1-y} remain similar with the pristine $IrO_{x(x>2)}$/oxi-TiN, while a slight increase in the overpotential is observed for all 1 to 3 ML model systems (**Figure S33**). In addition, the effect of solvation and surface charges was also tested for 2ML-$IrO_{x(x>2)}$/oxi-TiN.[31] The results showed that the explicit inclusion of acid environments did not affect the preference to AEM mechanism (**Figure 6i** and **S34**). Furthermore, the overpotential of 2ML-$IrO_{x(x>2)}$/oxi-TiN remained lower than that of IrO_2 (**Figure 6i**), consistent with experimental observations.

Conclusion

In summary, we developed a CO-assisted synthesized CO-IrO_x/oxi-TiN catalyst to increase the oxidation state of Ir, leading to an outstanding OER performance in acidic media with a low overpotential of 277 mV at 10 mA cm^{-2} and a high mass activity of 542 A g_{Ir}^{-1}. When the CO-IrO_x/oxi-TiN catalyst is integrated into a PEM water electrolyzer with a low Ir-loading of 0.26 mg cm^{-2}, it achieves a current density of 2.4 A cm^{-2} at 1.8 V, outperforming EtOH-IrO_x/oxi-TiN (2.0 A cm^{-2}) and C-IrO_2 (1.2 A cm^{-2}). Based on *in situ* XAS analysis and DFT calculations, we conclude that enhanced activity originates from the high oxidation state of $Ir^{\delta+}$ ($\delta > 4$) under OER conditions. DFT calculations further confirm that when using the oxygen-modified TiN as the support, the interfacial stoichiometry of O relative to Ir is increased, and therefore the $IrO_{x(x>2)}$/oxi-TiN model shows the highest oxidation state and the lowest OER overpotential. DFT calculations reveal that the oxidation state of Ir is shown to be an activity descriptor, with higher oxidation states being associated with smaller OER overpotentials. This study emphasizes the correlation between the high oxidation state of $Ir^{\delta+}$ and high OER activity, providing guidance for designing more active acidic OER catalysts.

Supporting Information

The authors have cited additional references within the Supporting Information. [11, 31-53]

Acknowledgements

This work was financially supported by the Division of Chemical Sciences, Geosciences, & Biosciences, Office of Basic Energy Sciences, Department of Energy (Grant number DE-SC0012704 with BNL FWP CO-060). This research used resources of the Center for Functional Nanomaterials (CFN) and beamlines 7-BM (QAS) of the National Synchrotron Light Source II (NSLS-II) at Brookhaven National Laboratory (Contract No. DE-SC0012704 and DE-SC0012653), U.S. DOE Office of Science User Facilities. Beamline operations were supported in part by the Synchrotron Catalysis Consortium (U.S. DOE, Office of Basic Energy Sciences, Grant No. DE-SC0012335). DFT calculations in this work were performed using computational resources at Center for Functional Nanomaterials (CFN), and the Scientific Data and Computing Center, a component of the Computational Science

Initiative, at Brookhaven National Laboratory under Contract No. DE-SC0012704, and at the National Energy Research Scientific Computing Center (NERSC), a DOE Office of Science User Facility, supported by the Office of Science of the DOE under contract DE-AC02-05CH11231.

[1] Y. Zhu, J. Wang, T. Koketsu, M. Kroschel, J.-M. Chen, S.-Y. Hsu, G. Henkelman, Z. Hu, P. Strasser, J. Ma, *Nature Communications* **2022**, *13*, 7754.

[2] M. Zlatar, D. Escalera-López, M. G. Rodríguez, T. Hrbek, C. Götz, R. Mary Joy, A. Savan, H. P. Tran, H. N. Nong, P. Pobedinskas, V. Briega-Martos, A. Hutzler, T. Böhm, K. Haenen, A. Ludwig, I. Khalakhan, P. Strasser, S. Cherevko, *ACS Catalysis* **2023**, *13*, 15375-15392.

[3] Q. Wang, Y. Cheng, H. B. Tao, Y. Liu, X. Ma, D.-S. Li, H. B. Yang, B. Liu, *Angewandte Chemie International Edition* **2023**, *62*, e202216645.

[4] S. Kong, A. Li, J. Long, K. Adachi, D. Hashizume, Q. Jiang, K. Fushimi, H. Ooka, J. Xiao, R. Nakamura, *Nature Catalysis* **2024**, *7*, 252-261.

[5] Q. Dang, H. Lin, Z. Fan, L. Ma, Q. Shao, Y. Ji, F. Zheng, S. Geng, S.-Z. Yang, N. Kong, W. Zhu, Y. Li, F. Liao, X. Huang, M. Shao, *Nature Communications* **2021**, *12*, 6007.

[6] L. C. Seitz, C. F. Dickens, K. Nishio, Y. Hikita, J. Montoya, A. Doyle, C. Kirk, A. Vojvodic, H. Y. Hwang, J. K. Norskov, T. F. Jaramillo, *Science* **2016**, *353*, 1011-1014.

[7] J. Gao, C.-Q. Xu, S.-F. Hung, W. Liu, W. Cai, Z. Zeng, C. Jia, H. M. Chen, H. Xiao, J. Li, Y. Huang, B. Liu, *Journal of the American Chemical Society* **2019**, *141*, 3014-3023.

[8] M. Retuerto, L. Pascual, J. Torrero, M. A. Salam, Á. Tolosana-Moranchel, D. Gianolio, P. Ferrer, P. Kayser, V. Wilke, S. Stiber, V. Celorrio, M. Mokthar, D. G. Sanchez, A. S. Gago, K. A. Friedrich, M. A. Peña, J. A. Alonso, S. Rojas, *Nature Communications* **2022**, *13*, 7935.

[9] X. Zheng, J. Tang, A. Gallo, J. A. Garrido Torres, X. Yu, C. J. Athanitis, E. M. Been, P. Ercius, H. Mao, S. C. Fakra, C. Song, R. C. Davis, J. A. Reimer, J. Vinson, M. Bajdich, Y. Cui, *Proc Natl Acad Sci USA* **2021**, *118*.

[10] A. Li, S. Kong, K. Adachi, H. Ooka, K. Fushimi, Q. Jiang, H. Ofuchi, S. Hamamoto, M. Oura, K. Higashi, T. Kaneko, T. Uruga, N. Kawamura, D. Hashizume, R. Nakamura, *Science* **2024**, *384*, 666-670.

[11] X. Han, T. Mou, A. Islam, S. Kang, Q. Chang, Z. Xie, X. Zhao, K. Sasaki, J. A. Rodriguez, P. Liu, J. G. Chen, *Journal of the American Chemical Society* **2024**, *146*, 16499-16510.

[12] C. Cui, L. Gan, M. Neumann, M. Heggen, B. Roldan Cuenya, P. Strasser, *Journal of the American Chemical Society* **2014**, *136*, 4813-4816.

[13] Y. Dai, X. Mu, Y. Tan, K. Lin, Z. Yang, N. Zheng, G. Fu, *Journal of the American Chemical Society* **2012**, *134*, 7073-7080.

[14] Y.-X. Tuo, L.-J. Shi, H.-Y. Cheng, Y.-A. Zhu, M.-L. Yang, J. Xu, Y.-F. Han, P. Li, W.-K. Yuan, *Journal of Catalysis* **2018**, *360*, 175-186.

[15] Z. Shi, J. Li, Y. Wang, S. Liu, J. Zhu, J. Yang, X. Wang, J. Ni, Z. Jiang, L. Zhang, Y. Wang, C. Liu, W. Xing, J. Ge, *Nature Communications* **2023**, *14*, 843.

[16] V. K. Puthiyapura, M. Mamlouk, S. Pasupathi, B. G. Pollet, K. Scott, *Journal of Power Sources* **2014**, *269*, 451-460.

[17] H.-S. Oh, H. N. Nong, T. Reier, M. Gliech, P. Strasser, *Chemical Science* **2015**, *6*, 3321-3328.

[18] Z. Shi, J. Li, J. Jiang, Y. Wang, X. Wang, Y. Li, L. Yang, Y. Chu, J. Bai, J. Yang, J. Ni, Y. Wang, L. Zhang, Z. Jiang, C. Liu, J. Ge, W. Xing, *Angewandte Chemie International Edition* **2022**, *61*, e202212341.

[19] G. Jiang, H. Yu, Y. Li, D. Yao, J. Chi, S. Sun, Z. Shao, *ACS Applied Materials & Interfaces* **2021**, *13*, 15073-15082.

[20] F. Gu, L. Zheng, H. Wei, W. Mi, C. Zhang, Q. Su, W. Zhu, W. Lin, *Applied Surface Science* **2022**, *606*, 155008.

[21] M. Long, S. Lai, K. Miao, W. Jiang, W. Fan, X. Kang, *Angewandte Chemie International Edition*, e202419956.

[22] Y. Zeng, X. Guo, Z. Shao, H. Yu, W. Song, Z. Wang, H. Zhang, B. Yi, *Journal of Power Sources* **2017**, *342*, 947-955.

[23] X. Duan, H. Liu, W. Zhang, Q. Ma, Q. Xu, L. Khotseng, H. Su, *Electrochimica Acta* **2023**, *470*, 143271.

[24] C. Lee, K. Shin, Y. Park, Y. H. Yun, G. Doo, G. H. Jung, M. Kim, W. C. Cho, C. H. Kim, H. M. Lee, *Advanced Functional Materials* **2023**, *33*, 2301557.

[25] P. Lettenmeier, L. Wang, U. Golla-Schindler, P. Gazdzicki, N. A. Cañas, M. Handl, R. Hiesgen, S. S. Hosseiny, A. S. Gago, K. A. Friedrich, *Angewandte Chemie International Edition* **2016**, *55*, 742-746.

[26] J. Y. Lim, G. Rahman, S. Y. Chae, K.-Y. Lee, C.-S. Kim, O.-S. Joo, *International Journal of Energy Research* **2014**, *38*, 875-883.

[27] Y. Ping, R. J. Nielsen, W. Goddard, *Journal of the American Chemical Society* **2017**, *139*, 149-155.

[28] K. Klyukin, A. Zagalskaya, V. Alexandrov, *The Journal of Physical Chemistry C* **2018**, *122*, 29350-29358.

[29] X. K. Gu, J. C. A. Camayang, S. Samira, E. Nikolla, *Journal of Catalysis* **2020**, *388*, 130.

[30] I. C. Man, H. Y. Su, F. Calle-Vallejo, H. A. Hansen, J. I. Martínez, N. G. Inoglu, J. Kitchin, T. F. Jaramillo, J. K. Norskov, J. Rossmeisl, *Chemcatchem* **2011**, *3*, 1159-1165.

[31] T. Mou, D. A. Bushiri, D. V. Esposito, J. G. Chen, P. Liu, *Angewandte Chemie International Edition* **2024**, *63*, e202409526.

[32] D. Choi, P. N. Kumta, *Journal of The Electrochemical Society* **2006**, *153*, A2298.

[33] G. Kresse, J. Furthmüller, *Physical Review B* **1996**, *54*, 11169-11186.

[34] G. Kresse, J. Furthmüller, *Computational Materials Science* **1996**, *6*, 15-50.

[35] A. Hjorth Larsen, J. Jørgen Mortensen, J. Blomqvist, I. E. Castelli, R. Christensen, M. Dułak, J. Friis, M. N. Groves, B. Hammer, C. Hargus, E. D. Hermes, P. C. Jennings, P. Bjerre Jensen, J. Kermode, J. R. Kitchin, E. Leonhard Kolsbjerg, J. Kubal, K. Kaasbjerg, S. Lysgaard, J. Bergmann Maronsson, T. Maxson, T. Olsen, L. Pastewka, A. Peterson, C. Rostgaard, J. Schiøtz, O. Schütt, M. Strange, K. S. Thygesen, T. Vegge, L. Vilhelmsen, M. Walter, Z. Zeng, K. W. Jacobsen, *Journal of Physics: Condensed Matter* **2017**, *29*, 273002.

[36] B. Hammer, L. B. Hansen, J. K. Nørskov, *Physical Review B* **1999**, *59*, 7413-7421.

[37] J. D. Goodpaster, A. T. Bell, M. Head-Gordon, *The Journal of Physical Chemistry Letters* **2016**, *7*, 1471-1477.

[38] R. Sundararaman, W. A. Goddard, III, T. A. Arias, *The Journal of Chemical Physics* **2017**, *146*.

[39] K. Mathew, R. Sundararaman, K. Letchworth-Weaver, T. A. Arias, R. G. Hennig, *The Journal of Chemical Physics* **2014**, *140*, 084106.

[40] S. N. Steinmann, P. Sautet, *The Journal of Physical Chemistry C* **2016**, *120*, 5619-5623.

[41] Y. Wang, M. Zhang, Z. Kang, L. Shi, Y. Shen, B. Tian, Y. Zou, H. Chen, X. Zou, *Nature Communications* **2023**, 14, 5119.

[42] X. Zheng, M. Qin, S. Ma, Y. Chen, H. Ning, R. Yang, S. Mao, Y. Wang, *Advanced Science* **2022**, 9, 2104636.

[43] H. Ding, C. Su, J. Wu, H. Lv, Y. Tan, X. Tai, W. Wang, T. Zhou, Y. Lin, W. Chu, X. Wu, Y. Xie, C. Wu, *Journal of the American Chemical Society* **2024**, 146, 7858-7867.

[44] Z. Li, X. Li, M. Wang, Q. Wang, P. Wei, S. Jana, Z. Liao, J. Yu, F. Lu, T. Liu, G. Wang, *Advanced Materials* **2024**, 36, 2402643.

[45] S. Chen, S. Zhang, L. Guo, L. Pan, C. Shi, X. Zhang, Z.-F. Huang, G. Yang, J.-J. Zou, *Nature Communications* **2023**, 14, 4127.

[46] C. Shang, C. Cao, D. Yu, Y. Yan, Y. Lin, H. Li, T. Zheng, X. Yan, W. Yu, S. Zhou, J. Zeng, *Advanced Materials* **2019**, 31, 1805104.
[47] Z. Fan, Y. Ji, Q. Shao, S. Geng, W. Zhu, Y. Liu, F. Liao, Z. Hu, Y.-C. Chang, C.-W. Pao, Y. Li, Z. Kang, M. Shao, *Joule* **2021**, 5, 3221-3234.
[48] G. Li, K. Li, L. Yang, J. Chang, R. Ma, Z. Wu, J. Ge, C. Liu, W. Xing, *ACS Applied Materials & Interfaces* **2018**, 10, 38117-38124.
[49] S. Intikhab, M. Sokol, V. Natu, S. Chatterjee, Y. Li, M. W. Barsoum, J. Snyder, *Journal of Applied Electrochemistry* **2021**, 51, 1101-1108.
[50] Y. Wang, Z. Zhao, X. Liang, X. Zhao, X. Wang, S. Jana, Y. A. Wu, Y. Zou, L. Li, H. Chen, X. Zou, *Advanced Materials* **2024**, 36, 2407717.
[51] K. Zhang, W. Mai, J. Li, H. Wang, G. Li, W. Hu, *Journal of Materials Science* **2020**, 55, 3507-3520.
[52] D. Lebedev, R. Ezhov, J. Heras-Domingo, A. Comas-Vives, N. Kaeffer, M. Willinger, X. Solans-Monfort, X. Huang, Y. Pushkar, C. Copéret, *ACS Central Science* **2020**, 6, 1189-1198.
[53] K. Sun, X. Liang, X. Wang, Y. A. Wu, S. Jana, Y. Zou, X. Zhao, H. Chen, X. Zou, *Angewandte Chemie International Edition* **2025**, 64, e202504531.

Entry for the Table of Contents

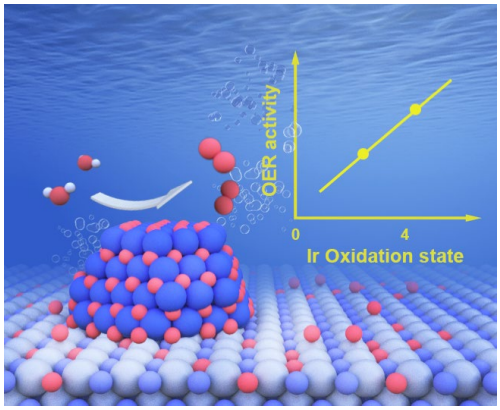

The IrO_x/oxi-TiN catalysts demonstrate a general correlation between iridium oxidation state and the oxygen evolution reaction activity.